Supporting Information

Northern Sourced Water dominated the Atlantic during the Last Glacial Maximum

F. Pöppelmeier[1], P. Blaser[1], M. Gutjahr[2], S. L. Jaccard[3], M. Frank[2], L. Max[4], J. Lippold[1]

[1]Institute of Earth Sciences, Heidelberg University, 69120 Heidelberg, Germany

[2]GEOMAR Helmholtz Center for Ocean Research Kiel, 24148 Kiel, Germany

[3]Institute of Geological Sciences and Oeschger Center for Climate Change Research, University of Bern, 3012 Bern, Switzerland

[4]MARUM-Center for Marine Environmental Sciences, University of Bremen, 28359 Bremen, Germany

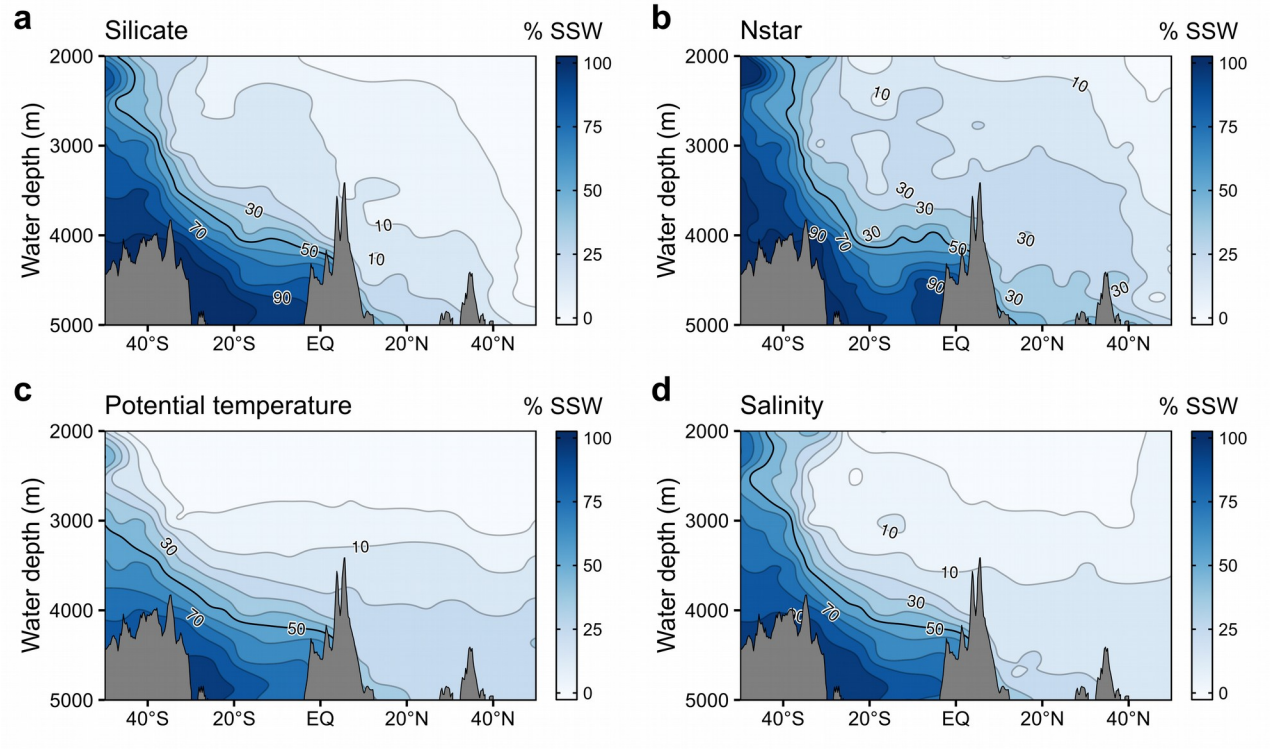

Figure S1: Southwest Atlantic hydrography. (a-d) Southern Sourced Water (SSW) contribution calculated from conservative hydrographic properties (silicate, N*, potential temperature, and salinity) of GEOTRACES transect GA02 (Schlitzer et al., 2018). N* was calculated from Nitrate and Phosphate concentrations according to N* = 0.87 * (N – 16P + 2.95µmol/l) (Gruber and Sarmiento, 1997). Fig 1A is the average of all four hydrographic properties plotted here. End member values from which % SSW were calculated are listed in Tab. S1.

Table S1: Hydrographic end members taken from the World Ocean Atlas (Garcia et al., 2014).

	Silicate (µmol/l)	**N* (µmol/l)**	**Pot. Temperature (°C)**	**Salinity (psu)**
NSW: 40.5°N/42.5°W – 3200 m	20.2	1.85	2.57	34.933
SSW: 55.5°S/21.5°W – 4000 m	118.8	-0.20	-0.33	34.658

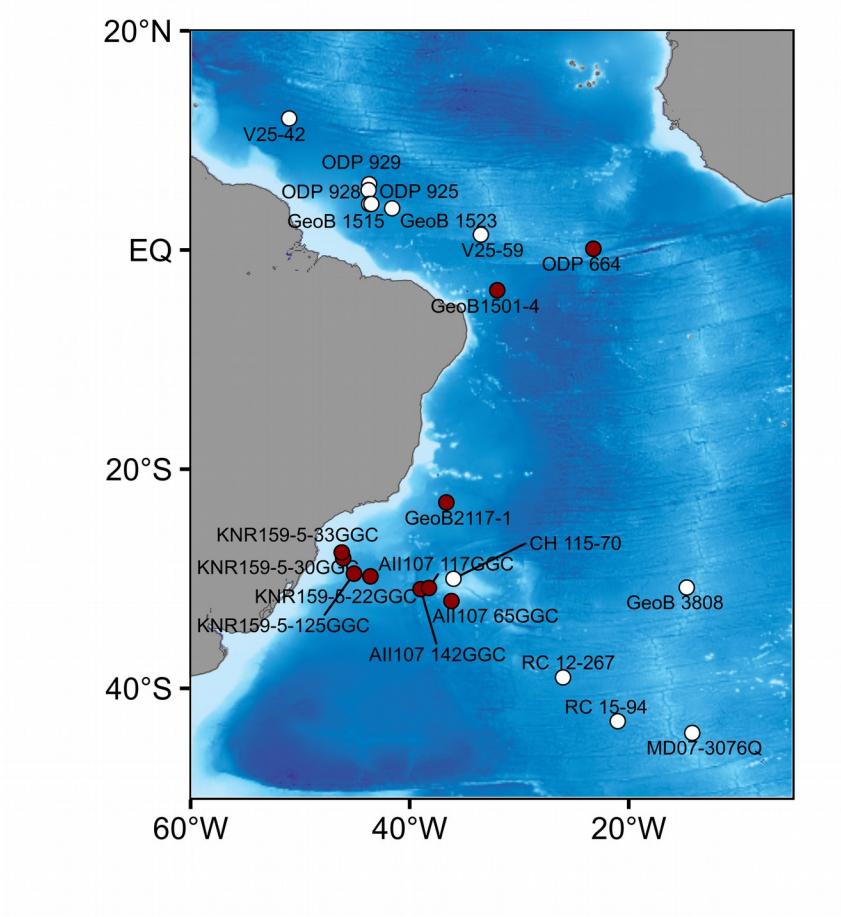

Figure S2: Core locations of sites used in this study. As described in the methods, only sites from the West Atlantic were considered to avoid any ambiguity caused by the different circulation geometries of the eastern and western basins. Details can be found in Tab. S2. Red circles mark new sites of this study.

Table S2: Core locations and references.

Site	Latitude (°N)	Longitude (°E)	Water depth (m)	Reference
AII107 117GGC	-30.84	-38.24	3282	this study
AII107 142GGC	-30.95	-39.00	4148	this study
AII107 65GGC	-32.03	-36.19	2795	Pöppelmeier et al. (2019)
CH 115-70	-30.00	-36.00	2340	Howe et al. (2016)
GeoB 1515	4.20	-43.70	3129	Lippold et al. (2016)
GeoB 1523	3.80	-41.60	3292	Lippold et al. (2016)
GeoB 3808	-30.80	-14.70	3213	Jonkers et al. (2015)
GeoB1501-4	-3.68	-32.01	4257	this study
GeoB2117-1	-23.04	-36.65	4045	this study
KNR159-5-125GGC	-29.53	-45.08	3589	this study
KNR159-5-22GGC	-29.78	-43.58	3924	this study
KNR159-5-30GGC	-28.13	-46.07	2500	Pöppelmeier et al. (2019)
KNR159-5-33GGC	-27.60	-46.20	2082	Pöppelmeier et al. (2019)
MD07-3076Q	-44.07	-14.20	3770	Skinner et al. (2013)
ODP 664	0.11	-23.23	3806	this study
ODP 925	4.20	-43.50	3040	Howe et al. (2016)
ODP 928	5.46	-43.75	4012	Howe et al. (2016)
ODP 929	6.00	-43.70	4360	Howe et al. (2016)
RC 12-267	-39.00	-26.00	4144	Howe et al. (2016)
RC 15-94	-43.00	-21.00	3762	Howe et al. (2016)
V25-42	12.00	-51.00	4707	Howe et al. (2016)
V25-59	1.40	-33.50	3824	Howe et al. (2016)

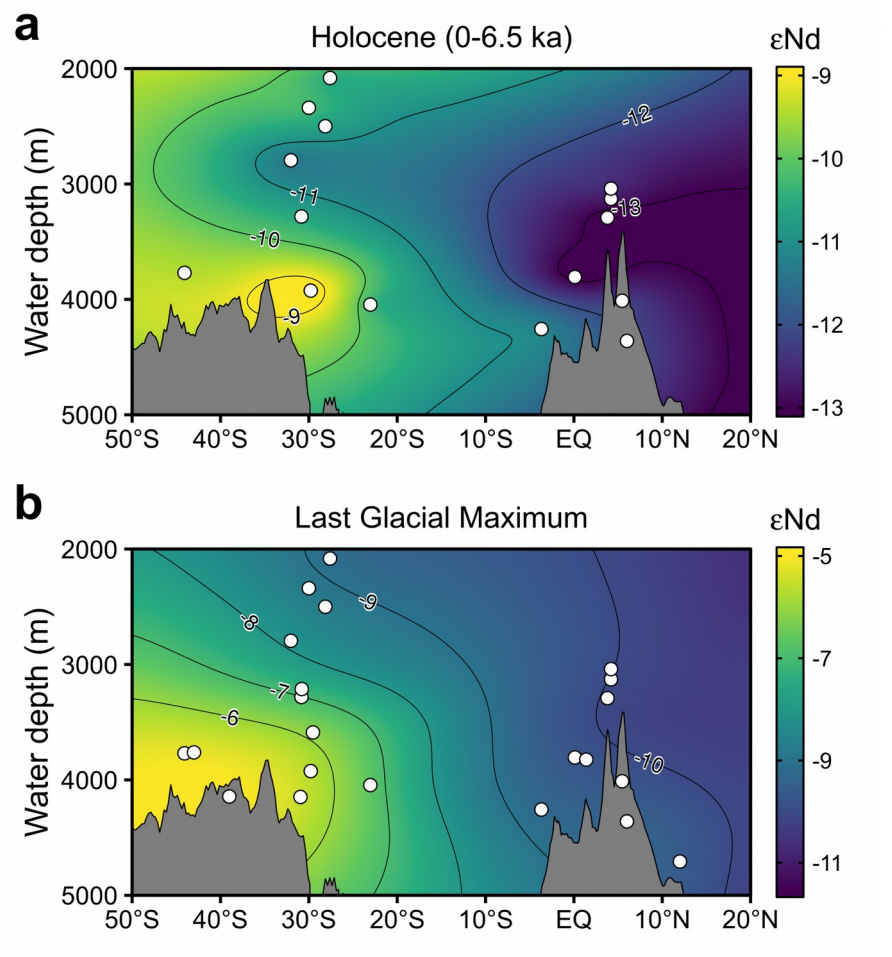

Figure S3: εNd section plots of the West Atlantic. (a) The mid to late Holocene (0-6.5 ka) and **(b)** Last Glacial Maximum (LGM). End members have been adjusted for the LGM panel, because the εNd end member shifted as discussed in the main text. White circles depict the locations of core sites also shown in Fig. 1. Some sediment cores have core tops older than 6.5 ka and are therefore not shown in panel a.

Calculation of percent Southern Sourced Water (% SSW) from εNd reconstructions:

The % SSW was calculated from a binary mixing model which follows as:

$$\%\,SSW = \frac{[Nd]_N(\varepsilon Nd - \varepsilon Nd_N)}{[Nd]_N(\varepsilon Nd - \varepsilon Nd_N) + [Nd]_S(\varepsilon Nd_S - \varepsilon Nd)} \times 100$$

Where $[Nd]_N$, εNd_N and $[Nd]_S$, εNd_S are the Nd concentration and isotope end members of the northern and southern sourced water masses, respectively. For the comparison with hydrographic properties (Fig. 2A) we used the modern seawater εNd and [Nd] end member values (van de Flierdt et al., 2016). For the LGM calculations we chose the εNd end members according to published reconstructions (Gu et al., 2019; Gutjahr et al., 2008; Huang et al., 2020; Skinner et al., 2013; Zhao et al., 2019) but assumed the Nd concentrations to be constant. All Nd end member properties are listed in Table S3.

For the LGM the largest uncertainties of this calculation stem from the unknown Nd concentrations of the end members, the only poorly constrained northern glacial εNd end member, and the measurement uncertainty at each site. It is possible that past Nd concentrations were different from today, but in contrast to past εNd reconstructions, at present no proxy exists for past seawater Nd

concentrations. The modern Nd concentrations of the global ocean indicate that deep water concentrations increase with ventilation ages since the poorly ventilated Pacific has higher Nd concentrations than the well ventilated Atlantic (cf. Lacan et al., 2012 versus van de Flierdt et al., 2016). The fact that the glacial Atlantic was more sluggish with ventilation ages about 700 – 1000 years higher than today (Skinner et al., 2017) could thus hint towards higher deep water Nd concentrations during the LGM. However, the higher glacial ventilation ages do not show a strong meridional trend, hence, changes in the ratio of NSW to SSW Nd concentrations were likely small. We estimate the uncertainty of the northern εNd end member to ± 1 ε-units which translates to an uncertainty in % SSW of about ± 10 % (in absolute terms). Finally, the measurement uncertainty of the reconstructed εNd accounts for an uncertainty in % SSW of about ± 5 %. The combined total uncertainty of our glacial % SSW calculations is therefore ± 15 %. For the Holocene εNd reconstructions the northern εNd end member is better constrained which reduces the total uncertainty in % SSW to ± 10 %.

Table S3: Nd end member properties.

	Nd concentration (pmol/kg)	**εNd**	**Reference**
NSW	18	-12.8	van de Flierdt et al. (2016)
Glacial NSW	18	-10.5	Zhao et al. (2019)
SSW	27	-9.0	Stichel et al. (2012); van de Flierdt et al. (2016)
Glacial SSW	27	-5.5	Skinner et al. (2013); Huang et al. (2020)

Site selection

New Nd isotope reconstructions are from sites located at the southern Brazil Margin, Rio Grande Rise, and western Tropical Atlantic at depths between 3000 and 4200 m (Figs. 1, S2). We focus on new and published data from sediment cores situated in the West Atlantic only because the main advection route for deep water is within the deep western boundary currents (Rhein et al., 2015). In addition, deep water can only enter the eastern basin through fracture zones, which produces a substantially different water mass distribution in the East Atlantic that does not display the same latitudinal water mass gradient as in the western Atlantic (Curry and Oppo, 2005). Sites situated north of 20°N are also not considered here because a recent study suggested that the benthic nepheloid layer of the North American basin influencing these locations (Bermuda Rise, Blake Ridge, and Corner Rise; Gardner et al., 2018) potentially alters the local bottom water and sedimentary Nd isotope signature (Pöppelmeier et al., 2019). While this local overprinting could be corrected for and the glacial influence of the benthic nepheloid layer seemed to be substantially weaker (Pöppelmeier et al., 2019), we exclude these data to avoid any ambiguity. Furthermore, we did not include εNd reconstructions from the Cape Basin since they are situated in the eastern Atlantic (Curry and Oppo, 2005; Howe et al., 2016), and because the high particle load of the local benthic nepheloid layer (Gardner et al., 2018) could potentially influence the local bottom water εNd, similar to the North American basin.

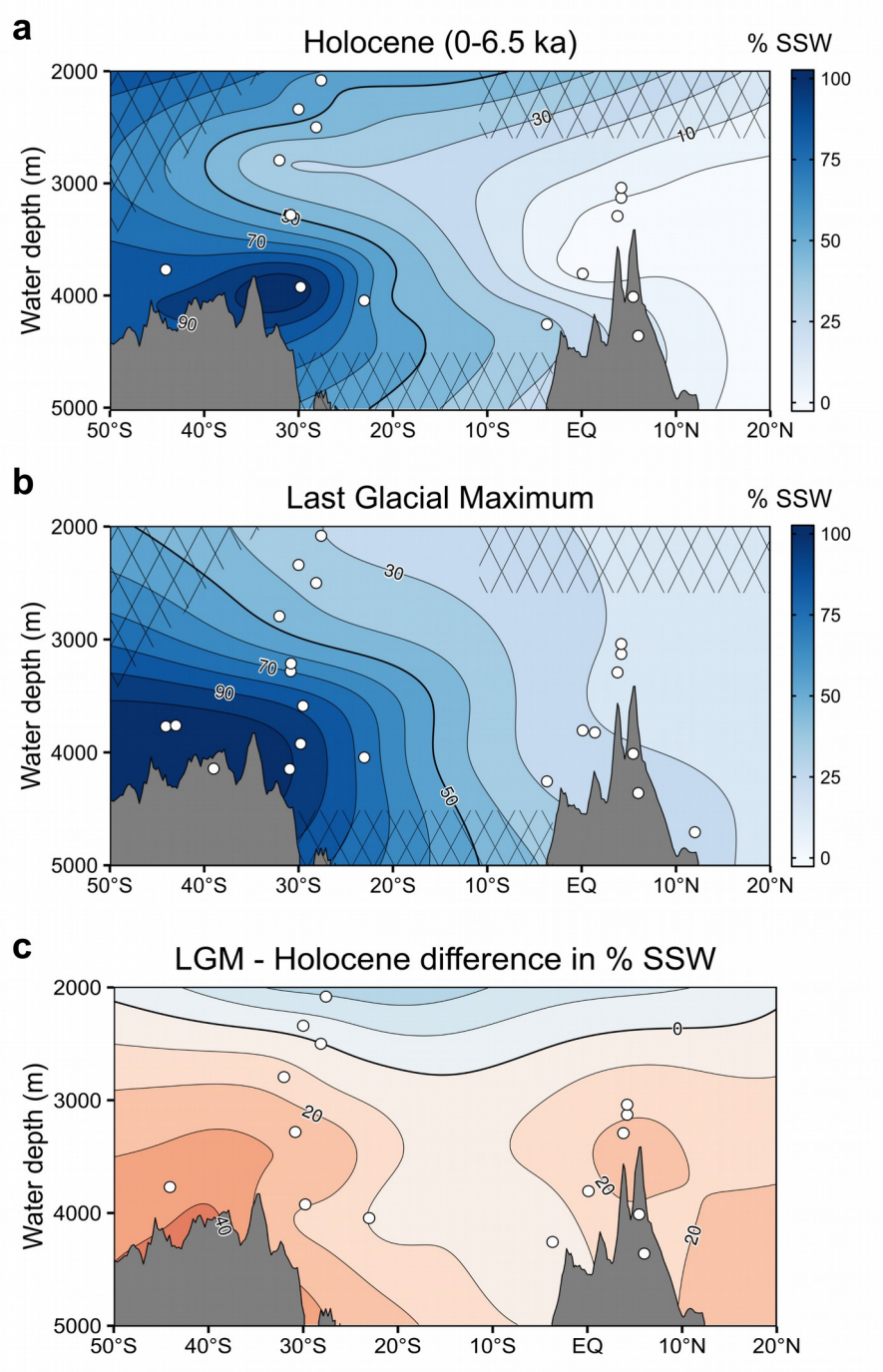

Figure S4: Water mass distribution during the Holocene and Last Glacial Maximum. (a) % Southern Sourced Water (% SSW) of the tropical and Southwest Atlantic during the mid to late Holocene. **(b)** Same as panel a but for the Last Glacial Maximum. Locations of sediment cores (white circles) are also marked in Fig. 1A. Inter- and extrapolation was performed with multilevel B-splines. Hatched areas mark regions with too little and/or no data points and are therefore unreliable. **(c)** Difference of % SSW between the Last Glacial Maximum (LGM) and Holocene based on the εNd calculations of panels a and b.

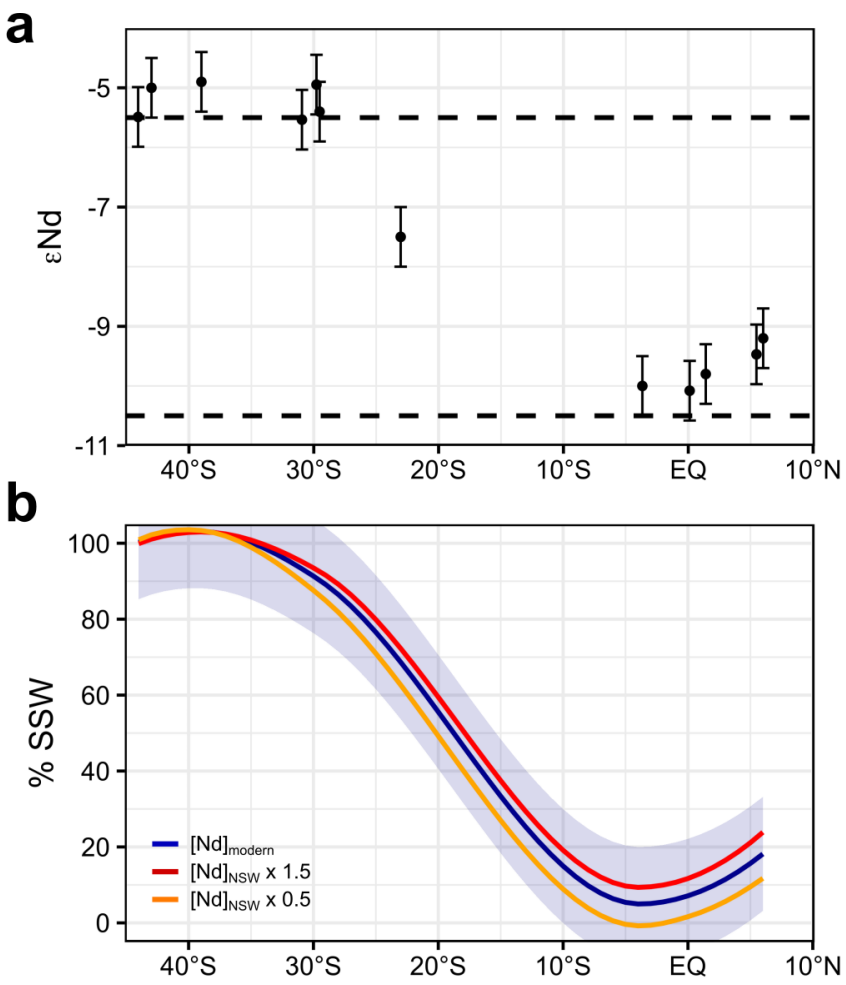

Figure S5: (a) All glacial εNd data along the meridional transect. Dashed lines mark the end member compositions (see Tab. S3). (b) Sensitivity of meridional water mass gradient derived from εNd on NSW Nd concentration of the LGM. Blue curve with uncertainty band is the same as in Fig. 2B and calculated with modern Nd end member concentration. Red and orange lines depict calculations where the NSW Nd concentration was increased and reduced by 50%, respectively.

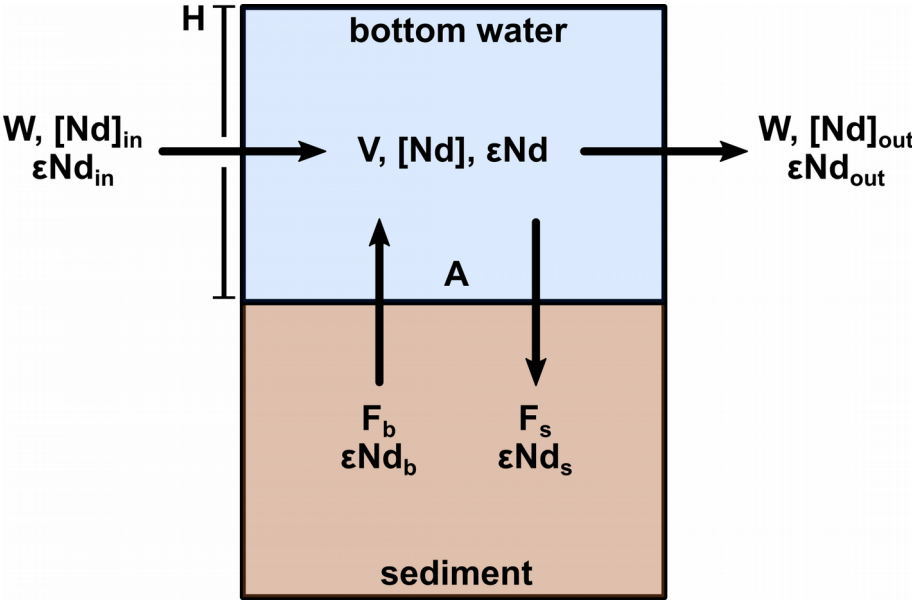

Figure S6: Schematics of the box model used to investigate the influence of a potential benthic flux on the εNd signature of SSW during the LGM. Results are shown in Figs. S7 and S8.

Description of Box Model:

We employ a simple box model (Fig. S6) to estimate the influence of a potential benthic flux on the Nd isotopic signature of Southern Sourced Water (SSW) on its northward path from the Rio Grande Rise to the equatorial Atlantic during the Last Glacial Maximum. We consider a water mass with thickness H that is in contact with the sediment on an area A, thus the water mass influenced by the potential benthic flux has a volume V = H * A. To consider Nd mass conservation we added a sink term (i.e. particle scavenging) that balances the Nd added to the water mass by the benthic flux ($|F_s| = |F_b * A|$). Advection is only considered horizontally and conserves mass. Upward mixing with an overlying water mass is neglected here. This gives:

$$\varepsilon Nd = \left(\varepsilon Nd_{in}[Nd]V + \varepsilon Nd_b F_b A + \varepsilon Nd_{in}[Nd]_{in} W - \varepsilon Nd_s F_S - \varepsilon Nd_{out}[Nd]_{out} W\right) / M_{Nd}$$

Where the εNd value within the box is the mass-normalized (M_{Nd}) sum of the initial εNd value weighted with the Nd concentration, the added Nd with signature εNd_b through the benthic flux F_b times the contact area, advected Nd $[Nd]_{in}$ with the flux W and isotopic composition εNd_{in}, and the two loss terms, due to particle scavenging removing Nd with a flux F_s and signature εNd_s as well as advection $\varepsilon Nd_{out} * [Nd]_{out}$. εNd_s and εNd_{out} equal the εNd value of the box from the previous iteration (initial values are same as εNd_{in}). The model was run until steady state was reached.

Table S4: Model parameters.

Variable	**Value**	**Reference**
Height: H	2000 m	assumed
Area: A	4.5×10^{12} m^2	Menard and Smith (1966)
Volume: V	9×10^{15} m^3	calculated
Nd concentration: [Nd]	27 pmol/kg	van de Flierdt et al. (2016)

Benthic flux: F_b	0-100 pmol/cm^2/yr	varied
εNd_{ini}	-5.5	this study
εNd_b	-7, -10	this study
Advection: W	2 – 8 Sv	varied

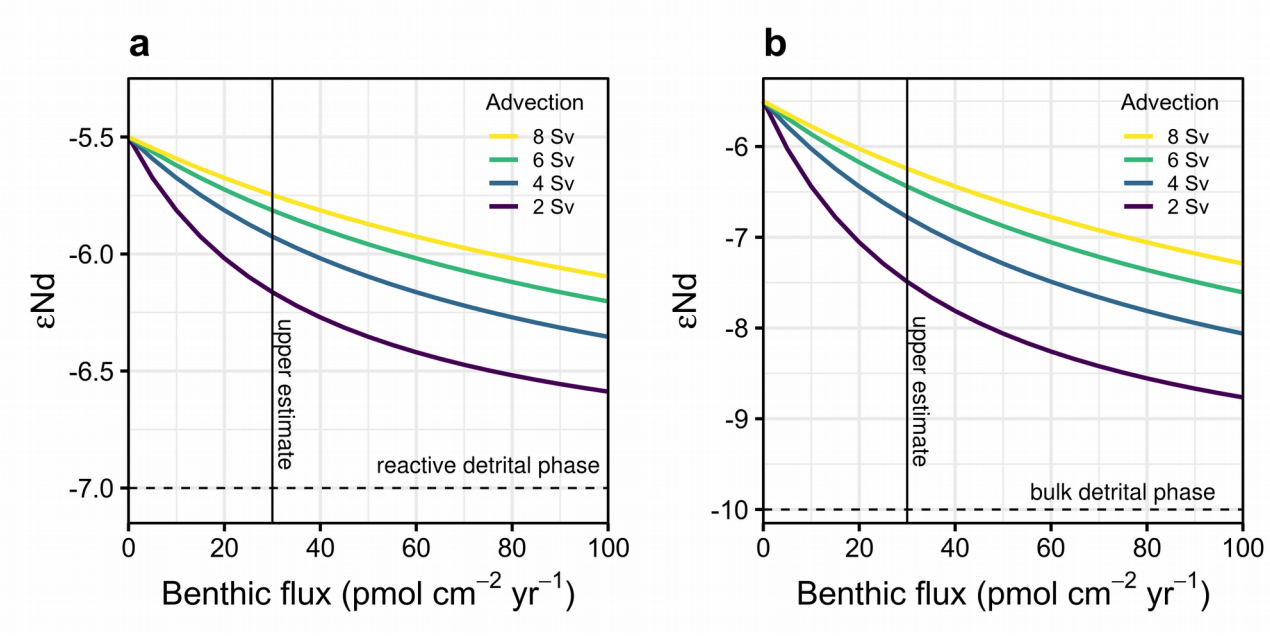

Figure S7: Influence of potential benthic flux during the LGM. (a) Non-conservative change of the Nd isotopic signature of SSW as a function of the strength of a potential benthic flux. Four different SSW current strengths are considered (2, 4, 6, and 8 Sverdrups; Sv = 10^6 m^3/s), with the maximum advection rate of 8 Sv corresponding to modern SSW strength (Talley et al., 2003). The Nd isotopic signature of the benthic flux is assumed to be the same as the reactive detrital phase identified in the sediment (Howe et al., 2018; Pöppelmeier et al., 2019). A benthic flux of 30 pmol/cm^2/yr was previously reported as the upper estimate at the Oregon Margin (Abbott et al., 2015). **(b)** Same as panel a, but with the benthic flux exhibiting the εNd signature of -10, same as the bulk detrital phase (Howe et al., 2018; Pöppelmeier et al., 2019). Note the different y-scales in both panels.

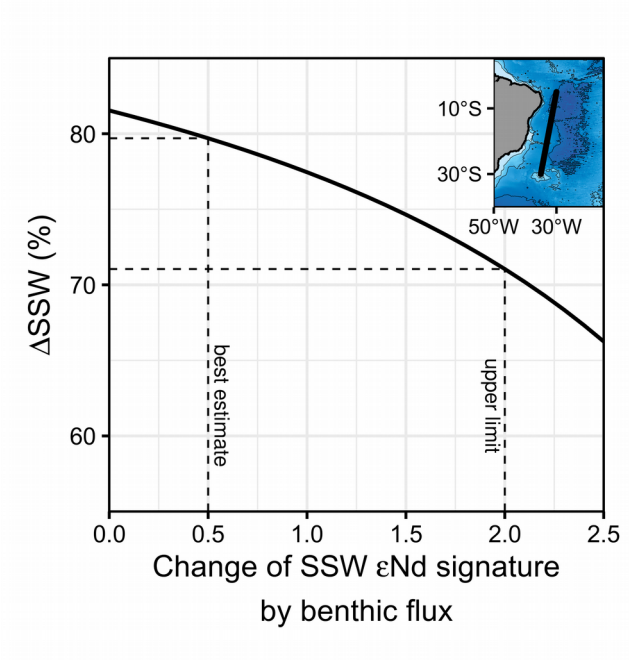

Figure S8: Influence of a potential benthic flux on the water mass gradient calculated from εNd along the transect depicted in the inlay map. From Fig. S7 we estimate the non-conservative effect from a benthic flux to the εNd signature of AABW to be about 0.5 ε-units. The upper limit of 2 ε-units is only achievable with the benthic flux exhibiting the same Nd isotope signature as the bulk detritus and a circulation strength of only 2 Sv.

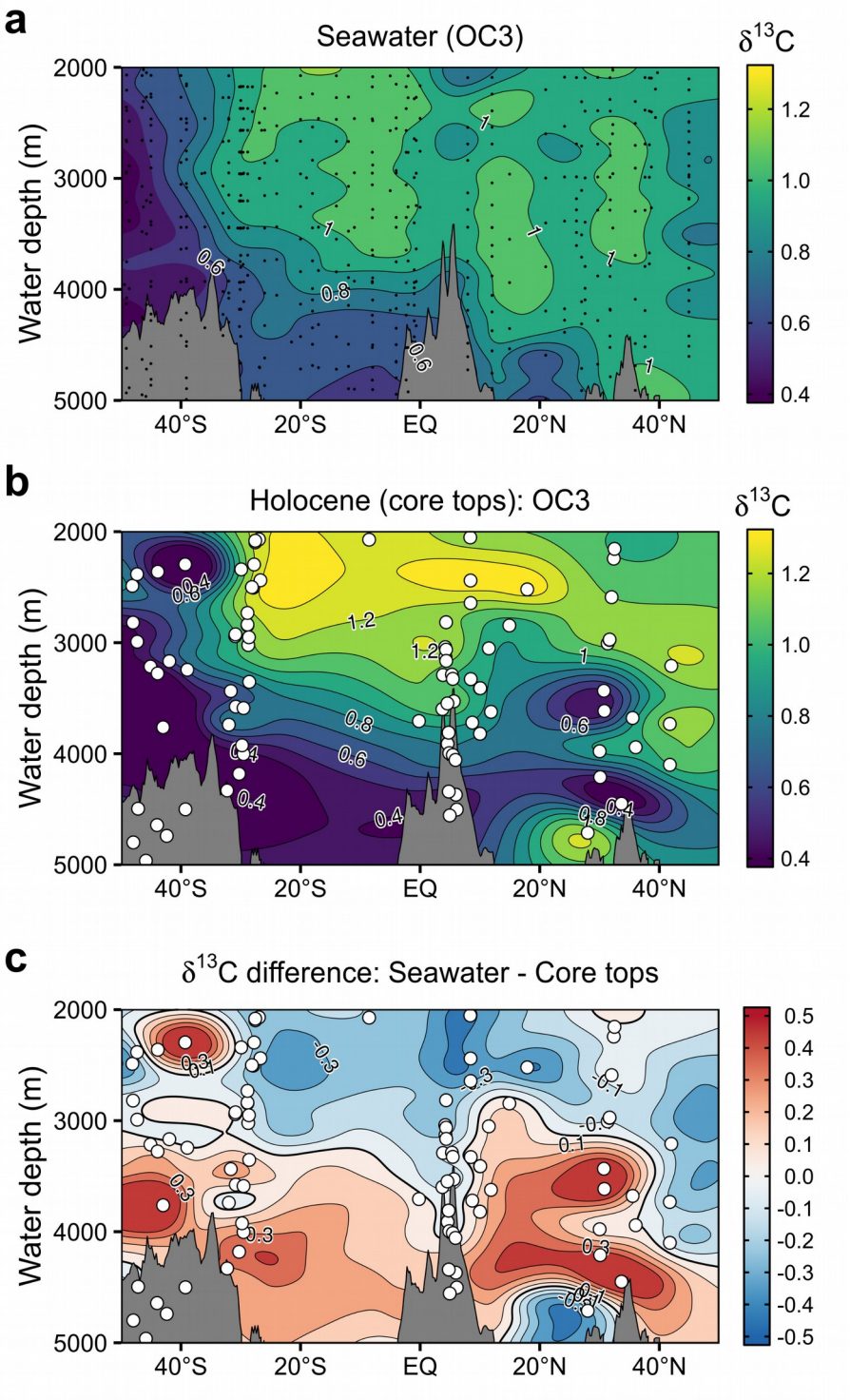

Figure S9: Stable carbon isotope compositions ($\delta^{13}C$) of **(a)** modern seawater and **(b)** core tops that represent the mid to late Holocene both compiled by the PAGES OC3 working group (Schmittner et al., 2017). **(c)** Difference between panels a and b.

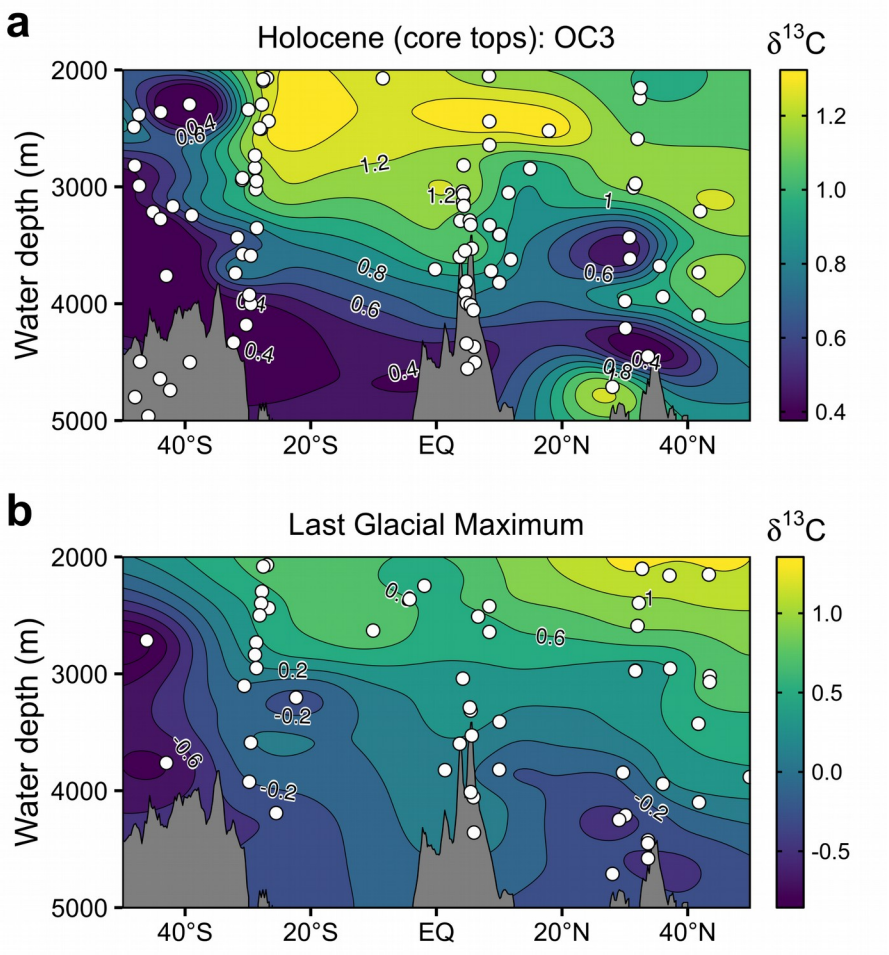

Figure S10: West Atlantic $\delta^{13}C$ of **(a)** Holocene-aged core tops (same as Fig. S9b; Schmittner et al., 2017), and **(b)** the Last Glacial Maximum (Oppo et al., 2018). Please note the different color scale in panel b.

References

Abbott, A. N., Haley, B. A., and McManuc, J. (2015). Bottoms up: Sedimentary control of the deep North Pacific Ocean's εNd signature. Geology v. 43, p. 1035-1038. doi:10.1130/G37114.1

Curry, W. B., & Oppo, D. W. (2005). Glacial water mass geometry and the distribution of $\delta^{13}C$ of CO_2 in the western Atlantic ocean. Paleoceanography 20 (1). doi:10.1029/2004PA001021

Garcia, H. E., et al (2014). World Ocean Atlas 2013, volume 4: Dissolved inorganic nutrients (phosphate, nitrate, silicate). In S. Levitus & A. Mishonov (Eds.), NOAA Atlas NESDIS 76 (25 pp.)

Gardner, W. D., Richardson, M. J., & Mishonov, A. V. (2018). Global assessment of benthic nepheloid layers and linkage with upper ocean dynamics. Earth and Planetary Science Letters 482, 126-134. doi:10.1016/j.epsl.2017.11.008

Gruber, N., & Sarmiento J. L. (1997). Global patterns of marine nitrogen fixation and denitrification. Global Biogeochemical Cycles 11:2, 235-266. doi:10.1029/97GB00077

Gu, S., Liu, Z., Jahn, A., Rempfer, J., Zhang, J., and Joos, F. (2019). Modeling neodymium isotopes in the ocean component of the CESM1. Journal of Advances in Modeling Earth Systems v. 11, p. 1-17. doi:10.1029/2018MS001538

Gutjahr, M., Frank, M., Stirling, C. H., Keigwin, L. D., & Halliday, A. N. (2008). Tracing the Nd isotope evolution of North Atlantic deep and intermediate waters in the western North Atlantic since the Last Glacial Maximum from Blake Ridge sediments. Earth and Planetary Science Letters 266 (1–2), 61–77. doi:10.1016/j.epsl.2007.10.037

Howe, J. N. W., Huang, K.-F., Oppo, D. W., Chiessi, C. M., Mulitza, S., Blusztajn, J., & Piotrowski, A. M. (2018). Similar mid-depth Atlantic water mass provenance during the Last Glacial Maximum and Heinrich Stadial 1. Earth and Planetary Science Letters 490, 51-61. doi:10.1016/j.epsl.2018.03.006

Howe, J. N. W., Piotrowski, A. M., Noble, T. L., Mulitza, S., Chiessi, C. M., & Bayon, G. (2016). North Atlantic deep water production during the Last Glacial Maximum. Nature Communications 7:11765. doi:10.1038/ncomms11765

Huang, H., Gutjahr, M., Eisenhauer, A., & Kuhn, G. (2020). No detectable Weddell Sea Antarctic Bottom Water export during the Last and Penultimate Glacial Maximum. Nature Communication v. 11:424. doi:10.1038/s41467-020-14302-3

Lacan, F., Tachikawa, K., and Jeandel, C. (2012). Neodymium isotopic composition of the oceans: A compilation of seawater data. Chemical Geology v. 300, p. 177-184. doi:10.1016/j.chemgeo.2012.01.019

Menard, H. W., & Smith, S. M. (1966). Hypsometry of ocean basin provinces. Journal of Geophysical Research v. 71, p. 4305-4325. doi:10.1029/JZ071i018p04305

Oppo, D. W., Gebbie, G., Huang, K.-F., Curry, W. B., Marchitto, T. M., & Pietro, K. R. (2018). Data constraints on glacial Atlantic water mass geometry and properties. Paleoceanography and Paleoclimatology 33:9, 1013-1034. doi:10.1029/2018PA003408

Pöppelmeier, F., et al. (2020). Water mass gradients of the mid-depth Southwest Atlantic during the past 25,000 years. Earth and Planetary Science Letters, 531. doi:10.1016/j.epsl.2019.115963

Schlitzer, R., et al. (2018). The GEOTRACES intermediate data product 2017. Chemical Geology 493, 210-223. doi:10.1016/j.chemgeo.2018.05.040

Schmittner, A., et al. (2017). Calibration of the carbon isotope composition ($\delta^{13}C$) of benthic foraminifera. Paleoceanography v. 32, p. 512-530. doi:10.1002/2016PA003072

Skinner, L. C., et al. (2017). Radiocarbon constraints on the glacial ocean circulation and its impact on atmospheric CO2. Nature Communications v. 8, p. 1-10. doi:10.1038/ncomms16010

Skinner, L. C., Scrivner, A. E., Vance, D., Barker, S., Fallon, S., & Waelbroeck, C. (2013). North Atlantic versus Southern Ocean contribution to a deglacial surge in deep ocean ventilation. Geology 41 (6), 667-670. doi:10.1130/G34133.1

Stichel, T., Frank, M., Rickli, J., Haley, B. A. (2012). The hafnium and neodymium isotope composition of seawater in the Atlantic sector of the Southern Ocean. Earth and Planetary Science Letters v. 317-318, p. 282-294. doi:10.1016/j.epsl.2011.11.025

Talley, L. D., Reid, J. L., & Robbins, P. E. (2003). Data-based meridional overturning streamfunctions for the global ocean. Journal of Climate v. 16, p. 3213-3226. doi:10.1175/1520-0442(2003)016<3213:DMOSFT>2.0.CO;2

van de Flierdt, T., Griffiths, A. M., Lambelet, M., Little, S. H., Stichel, T., Wilson, D. J. (2016). Neodymium in the oceans: a global database, a regional comparison and implications for palaeoceanographic research. Philosophical Transactions A 374 (2081). doi:10.1098/rsta.2015.0293

Zhao, N., Oppo, D. W., Huang, K.-F., Howe, J. N. W., Blusztajn, J., & Keigwin L. D. (2019). Glacial–interglacial Nd isotope variability of North Atlantic Deep Water modulated by North American ice sheet. Nature Communications v. 10:5773. doi:10.1038/s41467-019-13707-z